CANCER

Leukemia-on-a-chip: Dissecting the chemoresistance mechanisms in B cell acute lymphoblastic leukemia bone marrow niche

Chao Ma[1,2], Matthew T. Witkowski[3,4], Jacob Harris[2], Igor Dolgalev[3,4], Sheetal Sreeram[3], Weiyi Qian[1], Jie Tong[1], Xin Chen[1], Iannis Aifantis[3,4], Weiqiang Chen[1,2,4]*

B cell acute lymphoblastic leukemia (B-ALL) blasts hijack the bone marrow (BM) microenvironment to form chemoprotective leukemic BM "niches," facilitating chemoresistance and, ultimately, disease relapse. However, the ability to dissect these evolving, heterogeneous interactions among distinct B-ALL subtypes and their varying BM niches is limited with current in vivo methods. Here, we demonstrated an in vitro organotypic "leukemia-on-a-chip" model to emulate the in vivo B-ALL BM pathology and comparatively studied the spatial and genetic heterogeneity of the BM niche in regulating B-ALL chemotherapy resistance. We revealed the heterogeneous chemoresistance mechanisms across various B-ALL cell lines and patient-derived samples. We showed that the leukemic perivascular, endosteal, and hematopoietic niche-derived factors maintain B-ALL survival and quiescence (e.g., CXCL12 cytokine signal, VCAM-1/OPN adhesive signals, and enhanced downstream leukemia-intrinsic NF-κB pathway). Furthermore, we demonstrated the preclinical use of our model to test niche-cotargeting regimens, which may translate to patient-specific therapy screening and response prediction.

INTRODUCTION

B cell acute lymphoblastic leukemia (B-ALL) is the most common cancer among children and is characterized by the overproduction of immature and dysfunctional B cell blasts within bone marrow (BM). Despite the substantial progress achieved over the past decade with multidrug chemotherapy regimens, allogeneic hematopoietic stem cell (HSC) transplantation, and, most recently, CD19-targeted CAR (chimeric antigen receptor) T cell immunotherapy, relapse is common after initial treatment and the leading cause of death for pediatric patients with B-ALL (*1*, *2*). Patients with refractory and relapsed B-ALL have a poor prognosis with a 5-year survival rate of about 10%, largely because of acquired resistance by the heterogeneity in the BM microenvironment and tumor genetics (*1*–*3*). Currently, there is limited prognostic information between these heterogeneity and therapeutic responses, such as patients with *ETV6-RUNX1*$^+$ B-ALL often have favorable outcomes, while patients with Philadelphia chromosome–positive (*Ph*$^+$) B-ALL are expected to have an unfavorable prognosis (*4*). A clearer understanding of the microenvironmental evolution during leukemia pathogenesis and the heterogeneity of acquired chemoresistance mechanisms from distinct B-ALL subtypes may provide previously unidentified therapeutic targets for optimized therapy for patients with refractory and relapsed B-ALL.

The BM microenvironment is characterized by a complex milieu of evolving interactions among hematopoietic and nonhematopoietic niche cells to facilitate normal hematopoiesis. Upon leukemic initiation, B-ALL blasts transform their BM niches, dysregulating BM niche cell signaling to promote B-ALL pathogenesis and evade targeted therapies. Clinical ALL cases have reported abnormal vascular architecture in leukemic BM described by increased sinusoidal endothelial cell (EC) and perivascular mesenchymal stromal cell (MSC) proliferation, microvascular density and vascular permeability, and altered endosteal (osteoblastic) niche that together result in abnormal HSC and progenitor development and the accumulation of leukemia-associated factors (*5*). We, and others, have demonstrated in previous in vivo T cell ALL (T-ALL) studies that leukemia colonization is driven by CXCL12 (C-X-C motif chemokine ligand 12)/CXCR4 (C-X-C motif chemokine receptor 4) signals derived from the vascular niche (*6*, *7*). Leukemic blasts have also been shown to engage perivascular stromal cells or endosteal osteoblasts via intercellular adhesion mediated by, such as very late antigen–4 (VLA-4), vascular cell adhesion molecule–1 (VCAM-1) and osteopontin (OPN) (*8*–*10*). In addition, other hematopoietic cells, such as monocyte, may also be involved in regulating the chemotherapeutic response of B-ALL, as well as other types of leukemia (*11*–*13*). Moreover, HSCs residing in either endosteal region or medullary cavity demonstrate distinct niche-regulated cell fates (e.g., proliferation, quiescence, and differentiation) (*14*), suggesting that the perivascular and endosteal niches may differentially regulate B-ALL progression. These different niche cell components, cytokine and adhesive signaling, together can promote leukemia survival and/or dormancy, yet the downstream regulators remain not fully defined with transcription nuclear factor κB (NF-κB) being implied as a functional role (*8*–*10*). In addition, while the functions of perivascular and endosteal niches have been concurrent in healthy hematopoiesis and other leukemia types such as acute myeloid leukemia (AML), it remains poorly understood how B-ALL blasts may distinctly exploit BM microenvironment signaling to raise chemoresistance within these different BM niches (*15*–*17*).

To dissect the heterogeneity of BM niche mechanisms associated with treatment resistance for genetically distinct B-ALL subtypes, there is a critical demand for both an accurate, real-time, and modular methodology and reliable clinical biomarkers to identify and screen promising therapy targets for patients with refractory and relapsed B-ALL diseases. At present, preclinical ALL murine models, with the aid of intravital microscopy, have provided the foundation

[1]Department of Mechanical and Aerospace Engineering, New York University, Brooklyn, NY 11201, USA. [2]Department of Biomedical Engineering, New York University, Brooklyn, NY 11201, USA. [3]Department of Pathology, NYU Langone Health, New York, NY 10016, USA. [4]Perlmutter Cancer Center, NYU Langone Health, New York, NY 10016, USA.
*Corresponding author. Email: wchen@nyu.edu

of the in vivo leukemic BM ecology. Results emanating from these approaches may be difficult to reproduce as demonstrated, for instance, in previous T-ALL studies highlighting differences in leukemic blast localization in vivo (*6*, *7*, *18*) and translate to molecularly distinct B-ALL subtypes. The conventional two-dimensional (2D) or 3D cell coculture systems are simple and convenient platforms for biological studies but they cannot recapitulate the key architectures and characteristics of the in vivo B-ALL BM niche such as the central sinus, medullar cavity, and endosteal space as well as the hematopoietic environment (*19*, *20*). Moreover, scanning cell compositions in leukemic BM niches provides an overall demographic of BM cell populations, but it does not map the real-time and dynamic evolution of the tumor-niche cross-talk. Recent advances in microfluidics-based "organ-on-a-chip" in vitro models have been applied to mimic the pathophysiology of solid tumor microenvironments, yet few attempts have been made to accurately recapitulate the in vivo anatomical architectures and heterogeneity of the liquid tumors such as B-ALL, especially for revealing the heterogeneous resistance mechanisms (*21*–*24*).

In the present study, we reported an unique 3D organotypic "leukemia-on-a-chip" microphysiological system that maps the in vivo pathophysiology and heterogeneity of leukemic BM niches. Using this biomimetic system, we accurately characterized the mechanistic details of the real-time, dynamic interactions between B-ALL blasts and its leukemic BM niche within in vitro central sinus, medullary cavity, and endosteum anatomical regions as well as the hematopoietic environment. We also comparatively mapped the B-ALL subtype–specific niche signals with the integration of single-cell RNA sequencing (scRNA-seq) to further dissect the heterogeneity of leukemic niches using various genetically distinct human B-ALL cell lines and patient samples and validated that the niche-enhanced downstream NF-κB signaling and cellular quiescence in B-ALL blasts promote chemotherapy resistance. Last, we demonstrated the preclinical utility of our in vitro bioengineered model as a proof of concept to screen niche-cotargeting regimens, which together may translate to patient-specific therapeutics screening and disease management.

RESULTS

Modeling the in vivo leukemic BM niche in an in vitro leukemia-on-a-chip system

To mirror the in vivo pathology of the leukemic BM niche and identify underlying mechanisms responsible for B-ALL chemoresistance, we engineered an in vitro organotypic leukemic BM microenvironment, dubbed leukemia-on-a-chip. This microfluidics-based microphysiological system integrates key features that replicate in vivo BM tissue architecture and monitors dynamic B-ALL and leukemic BM niche interactions in real time with live-cell imaging (Fig. 1 and fig. S1). Specifically, leukemia-on-a-chip was fabricated using standard soft lithography with polydimethylsiloxane (PDMS) (*25*, *26*). Leukemia-on-a-chip culture (Fig. 1A and fig. S1, A to C) was compartmentalized into a central venous sinus (center region; red), a medullary cavity (middle ring; green), and endosteal regions (outer ring) connected with four medium reservoirs for long-term medium supply. These three functional regions were partitioned by regularly spaced trapezoid micropillars that confine cell-embedded hydrogels, by balancing surface tension and capillary forces, to overall mimic the native in vivo BM tissue architecture of leukemia.

The reconstituted on-chip leukemic BM niche houses a biomimetic central venous sinus, medullary cavity, and endosteum anatomical (endosteal) regions (Fig. 1B and fig. S1, D to F) that permit spatially defined, intercellular communication (i.e., B-ALL, ECs, MSCs, and osteoblasts) to interrogate cytokine and adhesive signaling milieus in conferring B-ALL chemoresistance. In parallel, we compared our on-chip reconstruction of the B-ALL BM niche to the in vivo BM tissue architecture of recipient mice injected with leukemic blasts, specifically using a high-risk Ph^+ B-ALL preclinical C57BL/6 mouse model (Fig. 1C) (*27*). Our results demonstrate that leukemia-on-a-chip resembles the in vivo spatial architecture and cellular composition of the leukemia BM tissue.

Mapping the leukemia niche heterogeneity across molecularly distinct B-ALL subtypes

Notably, interpreting the liaison between tumor heterogeneity and therapeutic response, such as patients with *ETV6-RUNX1*$^+$ B-ALL are associated with favorable outcome while patients with Ph^+ B-ALL display poor responses to conventional agents, as compared to tyrosine kinase inhibitor [e.g., nilotinib (NIL)], is still an outstanding issue (*4*). Moreover, because of the technical difficulties associated with isolating human BM stromal subpopulations in primary leukemic patient BM samples, the evolving interactions between human BM microenvironment and leukemia remain unclear. To study the heterogeneity in B-ALL human BM microenvironments, we used the leukemia-on-a-chip platform to established human B-ALL BM niche in vitro models by seeding either *ETV6-RUNX1*$^+$ REH [American Type Culture Collection (ATCC)] and Ph^+ SUP-B15 (SUP, ATCC) human B-ALL cell lines with a combination of human umbilical vein ECs (HUVECs; Lonza), human mesenchymal stem cells (hMSCs; Lonza), and human osteoblasts (hFOB 1.19, ATCC) that aimed to mimic components of the human BM niche. Notably, REH and SUP BM niches showed distinct chemotherapy sensitivity in the biomimetic devices upon exposure to increasing doses of vincristine (VCR; Sigma-Aldrich), with SUP B-ALL cocultured with niche cells showing more resistant to VCR than REH cocultured with niche cells (Fig. 1D), consistent with insensitivity of Ph^+ B-ALL to conventional chemotherapeutic agents. To understand the differences in chemosensitivity that exists between human B-ALL cell lines, SUP and REH, cocultured with BM niche cells, we quantified differences in cytokines present in the supernatant of these respective devices. Here, we showed that progressive production of CCL2, CCL5, interleukin-6 (IL-6), and IL-8 were observed upon seeding and growth of either REH or SUP in the leukemia BM niche model and that SUP BM niche had a slightly higher production of CCL2, IL-6, and IL-8, as compared to REH BM niche (Fig. 1E). We also observed that NF-κB signaling was enhanced in both leukemia subtypes upon coculture with niche cells (Fig. 1F), based on the nuclear/cytoplasmic expression of phosphorylated p65 subunit, a subunit of NF-κB. Moreover, we found that SUP B-ALL demonstrated a decreased percentage of Ki67 staining, whereas REH B-ALL showed an increased Ki67 expression, compared between with and without coculture with niche cells (Fig. 1G).

To further elucidate this heterogeneity across genetically distinct human B-ALL blasts and their related BM niches, we leveraged the powerful scRNA-seq analysis tool that we have recently reported for characterizing the BM microenvironment with limited cell input number (*11*, *28*) to molecularly explore the favorable (REH) and unfavorable (SUP) human leukemia BM niches. Single-cell suspensions

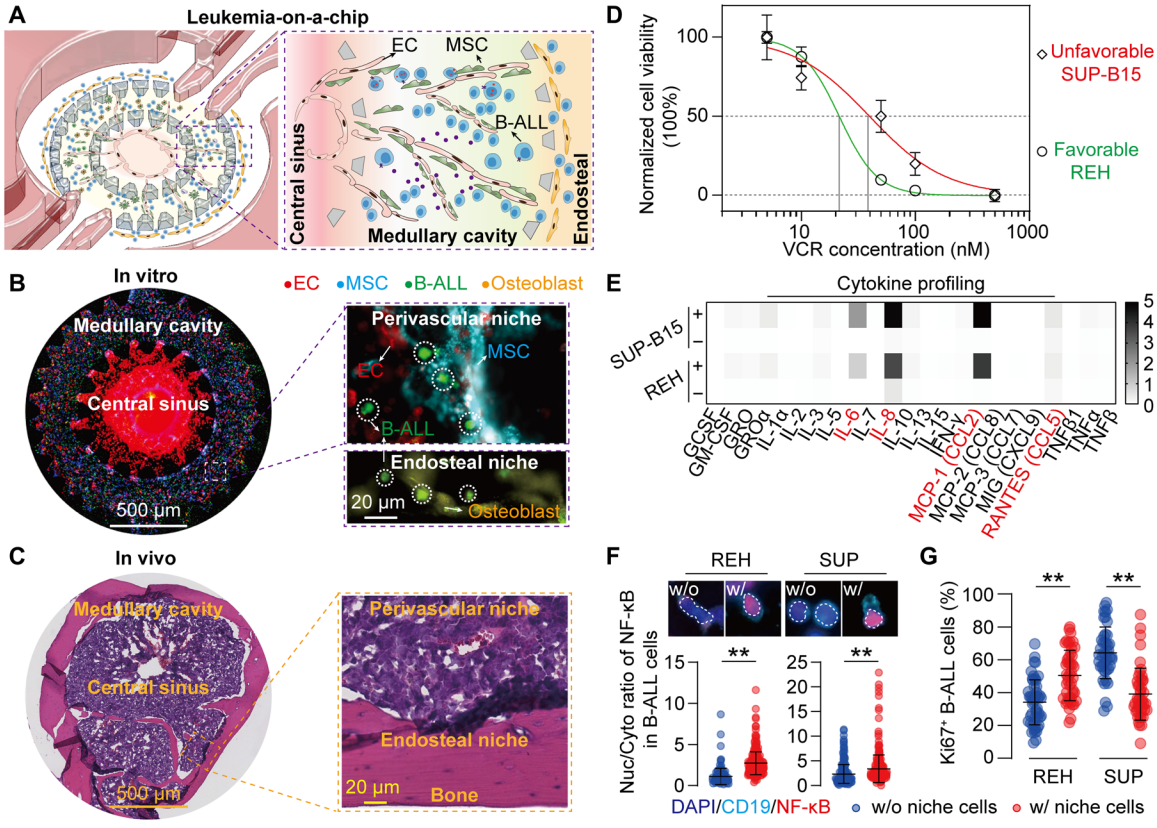

Fig. 1. Modeling the leukemic BM niche in a leukemia-on-a-chip platform. (**A**) Schematic demonstrating the design of leukemia-on-a-chip that consists of three functional regions. (**B**) Whole scan of the resultant leukemic BM niche system, where the enlarged area shows the colocalization of murine B-ALL cells within the perivascular niche. The bottom insert shows colocalization in the endosteal niche. (**C**) Hematoxylin and eosin (H&E) staining image of the in vivo murine leukemic BM niche, with the enlarged area showing the colocalization of B-ALL cells within the perivascular and endosteal niches. (**D**) The chemoresistance was compared between the engineered human BM niches of *ETV6-RUNX1*$^+$ REH and *Ph*$^+$ SUP-B15 B-ALL. Each drug concentration had three or more experimental replicates. (**E**) The cytokine profiles from two B-ALL blasts with and without niche cells were quantified using membrane-based enzyme-linked immunosorbent assay (ELISA) analysis. MCP-1, monocyte chemoattractant protein-1; MIG, monokine induced by gamma interferon. (**F**) Quantification of nuclear (Nuc)/cytoplasmic (Cyto) ratio of NF-κB in REH and SUP B-ALL within their respective niche models. The ratios for REH and SUP were manually measured from three experimental replicates ($n > 150$). (**G**) Percentage of Ki67$^+$ B-ALL cells, corresponding to (F). Data were collected from three experimental replicates. Unpaired *t* test (**$P < 0.01$, Mann-Whitney test). GCSF, granulocyte colony-stimulating factor; GM-CSF, granulocyte-macrophage colony-stimulating factor; GRO, growth-regulated oncogene; IL, interleukin; IFN-γ, interferon-γ; TGFβ1, transforming growth factor–β1; TNFα, tumor necrosis factor–α; DAPI, 4′,6-diamidino-2-phenylindole.

were prepared and sequenced for the engineered REH and SUP BM niche samples, as well as control groups (i.e., B-ALL alone and Niche alone) (Fig. 2A). In total, we obtained data for 14,650 cells (Fig. 2B). On the basis of the experimental design of input and culturing five distinct cell types (SUP B-ALL, REH B-ALL, osteoblasts, HUVECs, and hMSCs), we were able to classify single cells into five distinct clusters (Fig. 2, B and C) that distinctively expressed (REH and SUP B-ALL) *CD19*$^+$*PAX5*$^+$, (hMSC) *NES*$^+$, (osteoblasts) *COL1A1*$^+$, and (HUVECs) *CDH5*$^+$ (Fig. 2D). To further validate cell type identity of our niche cell clusters, we compared the gene signatures of our three niche cell clusters with previously described gene of murine BM niche cells (*28*). Together, these results confirmed that conserved gene signatures exist between previously described murine niche cell types and gene expression profiles of hMSC, osteoblasts, and HUVECs derived from our devices (fig. S2A).

We then performed gene sets enrichment analysis of Molecular Signature Database (MSigDB) Hallmark gene sets for all the cell types from the two leukemia niche samples (Fig. 2, E and F). We found that significantly enriched gene expression profiles related to TNFA signaling via NF-κB and inflammation response activation were associated with most of the cell types, highlighting the inflammation situation upon leukemia progression. SUP B-ALL, compared to REH B-ALL, significantly decreased expression of mitotic spindle and G_2-M checkpoint–related gene sets, which indicated that unfavorable B-ALL may demonstrate much more quiescence in comparison with favorable B-ALL in the leukemic BM niche (Fig. 2E). In contrast, niche cells from both leukemia niches augmented expression of epithelial mesenchymal transition–related gene sets, suggestive of leukemia-driven niche remodeling (Fig. 2F).

Having established gene expression profiles for the BM niche cells and leukemic blasts present in our in vitro devices, we sought to determine the cell type–specific and shared signaling pathways that exist throughout the leukemic microenvironments. In particular, we assessed the mRNA expression of leukemia survival and proliferation/quiescence regulators, such as *NFKB1A* and *MKI67* as well as niche-derived cytokine and adhesive signaling throughout all five clusters (Fig. 2 and fig. S2, B to D). In the presence of niche cells, for instance, we observed that SUP B-ALL blasts slightly decreased *MKI67* mRNA expression relative to those in the absence of niche cells, which is consistent with our on-chip observance (Fig. 1G and fig. S2B). In

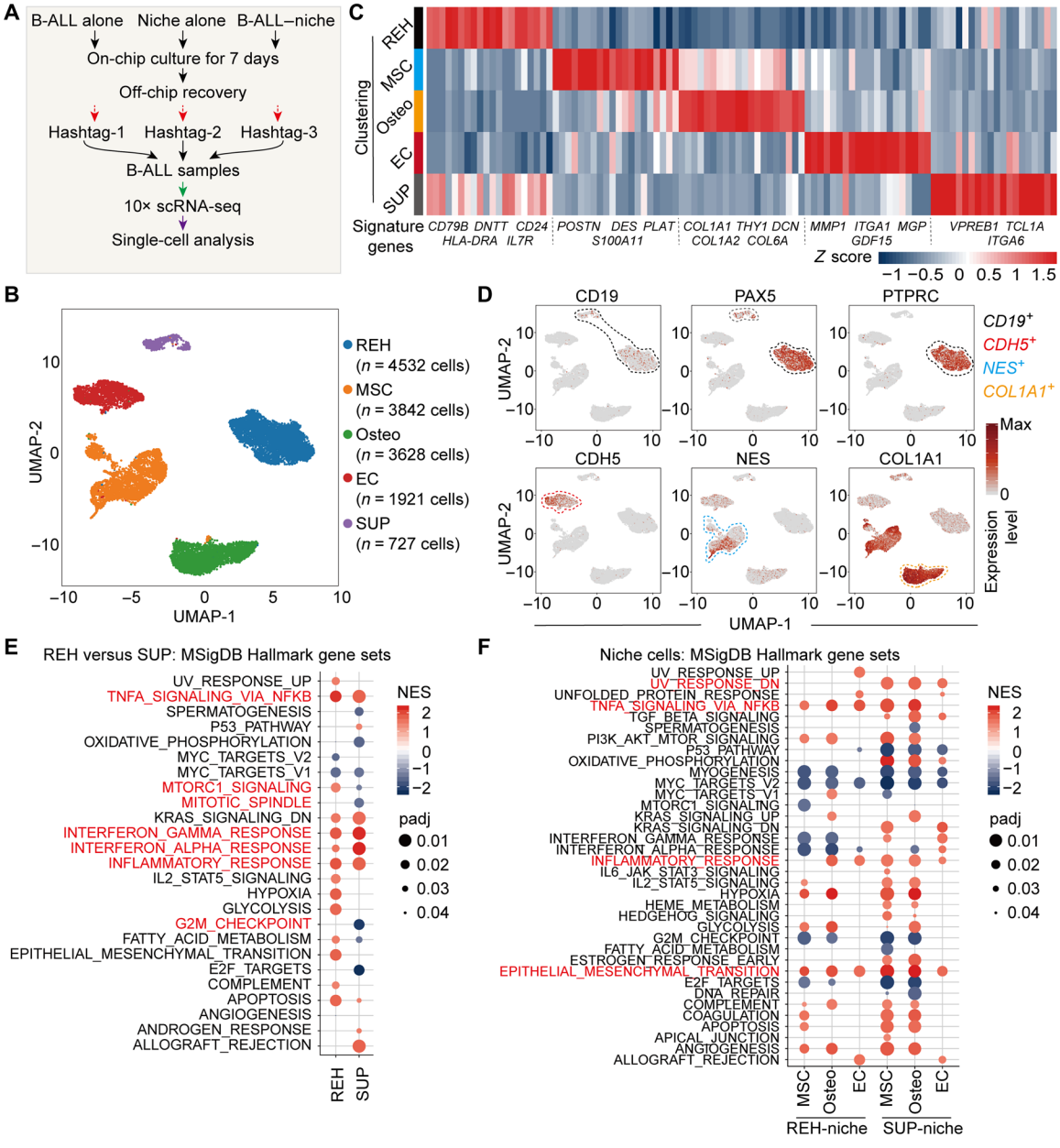

Fig. 2. scRNA-seq mapping of engineered human leukemic BM niches. (**A**) Study overview. (**B**) UMAP (uniform manifold approximation and projection) visualization of color-coded clustering of the leukemic niches. All cells can be grouped into five clusters: REH, SUP, hMSCs (MSC), HUVECs (EC), and osteoblasts (Osteo). (**C**) Gene signature of five clusters based on relative expression of the 20 most significant markers. Key genes are highlighted at the bottom. (**D**) Expression levels of lineage-specific genes via UMAP representation. Dashed lines encompass the examined *CD19*$^+$*PAX5*$^+$(black), *CDH5*$^+$ (red), *NES*$^+$ (cyan), and *COL1A1*$^+$ (yellow) populations. The *CD19*$^+$*PAX5*$^+$ populations can be divided into two subpopulations based on protein tyrosine PTPRC (protein tyrosine phosphatase receptor type C) expression. (**E** and **F**) MSigDB Hallmark gene set enrichment analysis. (E) The significantly enriched gene expression profiles that are related to TNFA signaling via NF-κB and inflammation response were present in both REH and SUP, while SUP but not REH significantly decreased expression of mitotic spindle and G_2-M checkpoint–related gene sets in leukemia niche models. (F) Comparative analysis of EC, MSC, and Osteo. Niche cells from both leukemia niches augmented expression of epithelial mesenchymal transition, inflammatory response, and TNFA signaling via NF-κB–related gene sets. Dot size represents adjusted *P* value (padj), with normalized enrichment score (NES) denoted by shade of color highlighted in the legend.

addition, SUP B-ALL cells increased *NFKB1A* expression when cultured with niche cells, whereas this was not the case for REH B-ALL. To clarify the variance of *NFKB1A* expression, we applied gene set enrichment analysis of *NF-κB* pathways on these two B-ALL cell types (fig. S2C). The results showed that both B-ALL blasts were more enriched with NF-κB–related signaling when cultured in leukemia BM niche models. As for gene expression of adhesive signaling in niche cells, we found that hMSCs from the SUP BM niche showed increased expression of OPN, while hMSCs from the REH BM niche showed decreased OPN expression, implicating that such heterogeneity may contribute to diverse extent of quiescence in the two leukemia subtypes (fig. S2D), although the protein levels may not fully correlate with the mRNA levels observed. Therefore, together with scRNA-seq, cytokine secretion, and immunofluorescence analysis,

we had generated a comprehensive molecular map of the engineered human BM niche for the two representative B-ALL cell types, which may provide a landscape to systematically interrogate the disease progression of varying leukemia subtypes and the accompanying transformation of nonmalignant BM niche components.

Monitoring the temporal dynamics of B-ALL progression in the leukemic niche

To mechanistically understand the dynamic microenvironmental interactions during leukemic pathogenesis, we longitudinally monitored the in situ migratory patterns of murine Ph^+ B-ALL and niche cells (containing ECs and MSCs) for a 3-day period with time-lapse imaging. To clearly visualize and distinguish Ph^+ GFP^+ leukemia cells and niche cells, we labeled ECs with CellTracker Red CMTPX dye (Thermo Fisher Scientific). We first characterized the migration of niche cells toward B-ALL cells by intentionally segregating niche cells into the ring area and B-ALL cells in the central region and mapped the dynamic migration of B-ALL cells and niche cells (especially ECs) at the interface of central and ring regions. We found that B-ALL cells attracted ECs during the 3-day culture, as indicated by the presence of ECs in the central area (Fig. 3A). In addition, we quantified the intercellular distance between B-ALL and niche cells during coculture, and the results demonstrated that B-ALL and niche cells dynamically colocalized (Fig. 3B). We further observed an enhanced clustering of B-ALL cells around niche cells compared to the B-ALL monoculture condition, indicating that niche cells may provide additional adhesive sites to facilitate B-ALL clustering (Fig. 3C). Time-lapse migration analysis of B-ALL cells revealed that leukemic cells either cultured in the presence or absence of niche cells were comparably motile at the culture onset (day 0), whereas after a two-day culture, leukemia blasts cocultured with niche cells were less motile, as compared to those cultured in the absence of niche cells (Fig. 3, D and E), suggesting the temporally evolved features in chemotactic and adhesive signaling among B-ALL blasts and niche cells. Together, these studies prove that in vivo B-ALL BM pathology is faithfully recapitulated in the in vitro leukemia-on-a-chip model that permits real-time and longitudinal monitoring of the in situ temporal microenvironmental evolution during leukemic pathogenesis, revealing unique migration patterns and clustering behaviors of B-ALL blasts in the leukemic BM niche.

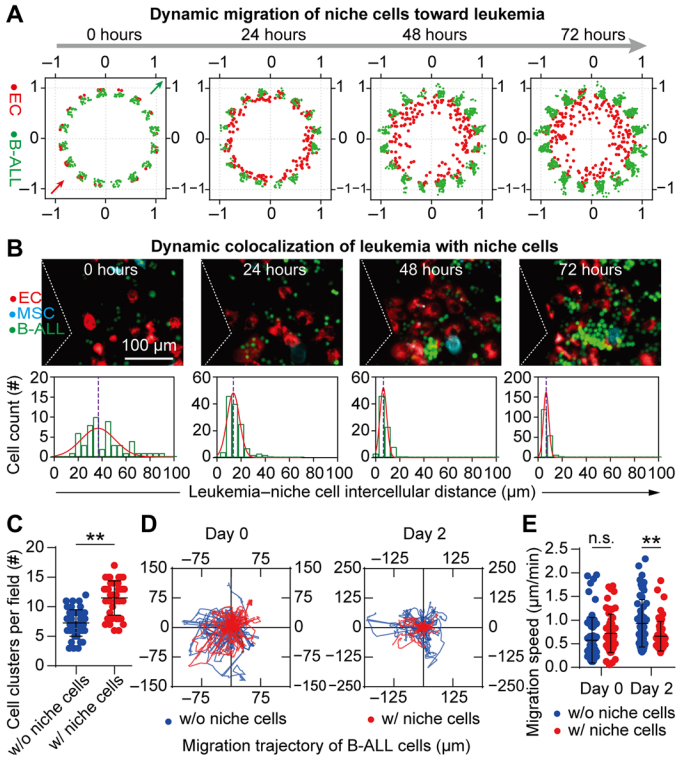

Fig. 3. Real-time monitoring of the leukemia–niche cell interaction dynamics. (**A**) Dynamic migration of niche cells (ECs) toward leukemia cells during 3-day culture. The result was extracted from one representative image within three experimental replicates. Scale bar, 1 cm. (**B**) Evolving dynamics of the murine leukemic BM niche during 3-day culture. The intercellular distances between leukemia and niche cells were manually quantified ($n > 50$) from three experimental replicates. The bin size at 5 was set for the histogram. (**C**) Clustering behavior of B-ALL cells cultured with or without niche cells. The B-ALL clusters (defined with at least 20 cells) were manually quantified from three experimental replicates. Unpaired *t* test (**$P < 0.01$, Mann-Whitney test). (**D**) The migration trajectory of individual B-ALL cells ($n = 60$) was recorded every 5 min over a period of 4 hours by time-lapse microscopy. In the flower plot diagram, the starting point of each track is placed at the axis origin. Data are representative of three individual experiments. (**E**) Average migration velocity (μm/min) of B-ALL cells of the indicated conditions analyzed in (D). Unpaired *t* test (n.s., not significant; **$P < 0.01$).

Dissecting the niche-derived signal underlying leukemia progression

We and others revealed in previous in vivo T-ALL and B-ALL studies that CXCL12 from BM niche may induce leukemia progression via its receptor CXCR4, thus supporting leukemia survival (*6*, *7*, *29*). To corroborate the results of scRNA-seq analysis of engineered leukemic BM niche, we studied the identified signaling further in our in vitro leukemia-on-a-chip model. We found that $CXCR4^+$ B-ALL cells were colocalized with $CXCL12^+$ niche cells in the leukemic BM niche (fig. S1G), confirming the potent role and the existence of spatiotemporal regulation of niche cell–derived signaling in the evolving progression of B-ALL. Steady-state cell surface expression of CXCR4 results from a balance between endocytosis, intracellular trafficking, and recycling (*30*). By quantifying the subcellular CXCR4 (Abcam, ab124824) receptor distribution in B-ALL cells, we showed that B-ALL cells in the B-ALL BM niche tended to have a higher ratio of CXCR4 internalized within the cytoplasm than those without niche cells, indicating active leukemia-intrinsic downstream events by CXCL12/CXCR4 signaling from interactions with the leukemic BM niche (Fig. 4, A and B). To confirm the source of CXCL12, we performed a membrane-based enzyme-linked immunosorbent assay (ELISA) cytokine analysis on niche cells (Fig. 4, C and D, and figs. S3 and S4). The results showed that niche cells (without culture with B-ALL blasts) exhibited high production of CXCL12, while it decreased within the leukemic niche upon 2-day coculture with B-ALL. This indicates that CXCL12 may function in the early stage of leukemia progression, such as induction of leukemia migration (Fig. 3, D and E). The overall cytokine profiles also demonstrated that niche cells secreted an array of cytokines, such as CCL2 and CCL5, regulating leukemia progression (figs. S3 and S4), which is consistent with our human system (Fig. 1E) and previous studies (*9*, *31*).

We also observed that leukemic blasts physically cluster around niche cells, indicating that niche cells may provide unique adhesion sites for engrafting B-ALL cells (Fig. 3C). HSC retention within the BM microenvironment is mediated by VLA-4/VCAM-1 signaling; similarly, leukemic blasts have been shown to engage perivascular

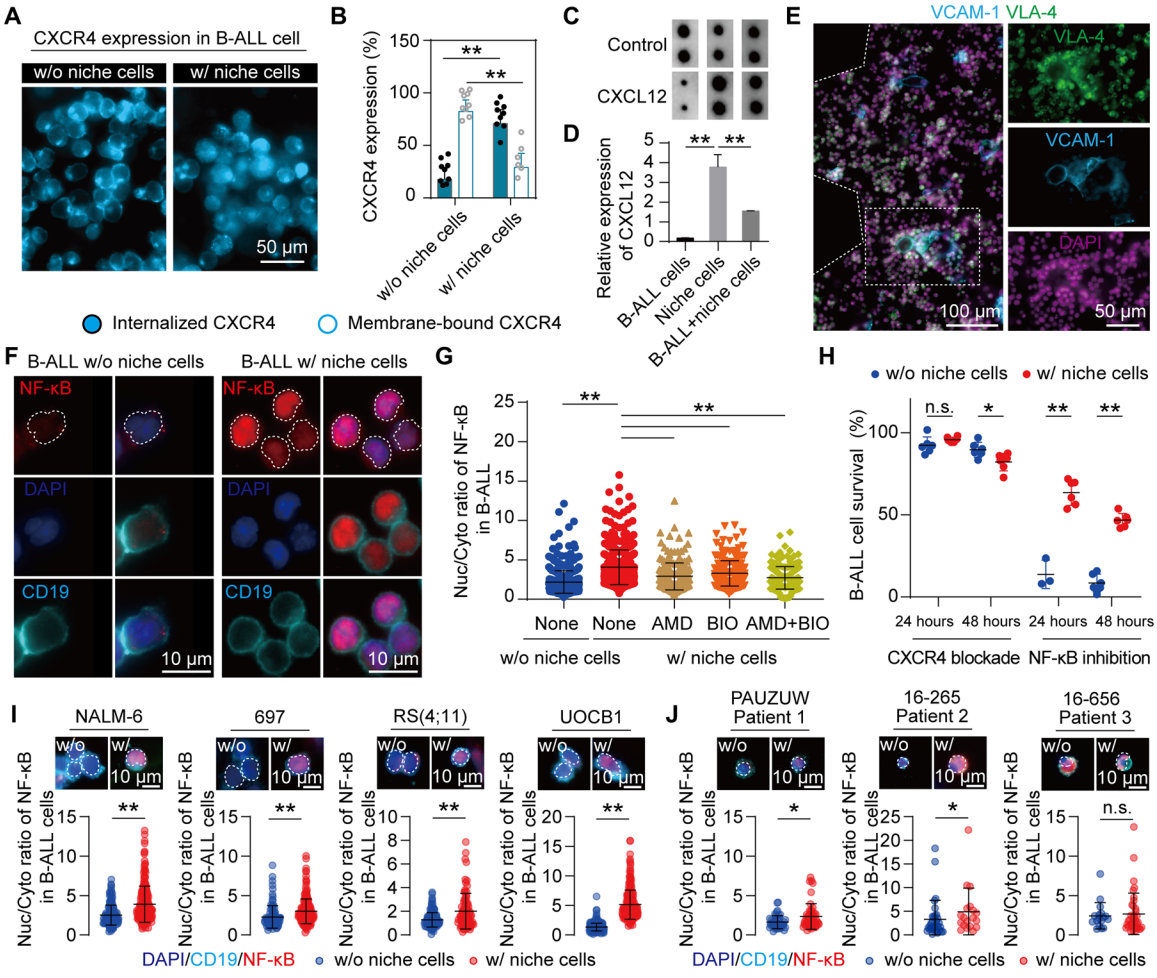

Fig. 4. Niche cells promoting leukemia progression via cytokine and adhesive signaling. (**A**) Regional CXCR4 distribution on murine B-ALL cells cultured with or without niche cells. (**B**) Quantified result corresponding to (A). (**C**) Membrane-based ELISA analysis of CXCL12 expression level of niche cells (ECs and MSCs). (**D**) Quantified result corresponding to (C). (**E**) Representative image showing B-ALL cells colocalized with niche cells via VCAM-1/VLA-4 signaling. (**F**) Representative images showing nuclear translocation of NF-κB in B-ALL cells. (**G**) NF-κB activation in B-ALL cells with or without niche cells and under treatments with CXCR4 inhibitor, AMD3100 (AMD), and VLA-4 inhibitor, BIO. The ratios were manually quantified from three experimental replicates ($n > 200$). One-way analysis of variance (ANOVA) followed by Tukey's post hoc test. (**H**) B-ALL cell viability cultured with or without niche cells. (**I**) Quantification of NF-κB activation in human NALM-6, 697, RS(4;11), and UOCB1 blasts within their leukemia niches. The ratios were manually measured from three experimental replicates ($N > 150$). (**J**) Quantification of NF-κB activation in patient-derived B-ALL blasts within engineered leukemia niches. The ratios for various B-ALL blasts were manually measured from three technical replicates ($N > 20$). Unpaired t test (*$P < 0.05$ and **$P < 0.01$, Mann-Whitney test).

stromal cells via this intercellular adhesive signaling (*8*–*10*). To confirm intercellular adhesive interactions between B-ALL cells and niche cells, we found, in on-chip cultures, that VLA-4$^+$ B-ALL cells (Abcam, ab202969) colocalized with VCAM-1$^+$ niche cells (Fig. 4E). In addition, we confirmed that blocking VLA-4 with BIO 5192 (BIO; R&D Systems) can significantly decrease the intercellular adhesion of B-ALL cells onto niche cells (fig. S5), proving that the niche cell–mediated VCAM-1/VLA-4 signaling is prominently involved in regulating B-ALL adhesion and clustering (Fig. 4E).

It remains not fully defined how these cytokine and adhesive signaling regulate B-ALL progression and chemoresistance. Previous evidence indicates that CXCR4 internalization and subsequent activation of phosphatidylinositol-3-OH kinase and Akt kinase lead to up-regulated NF-κB prosurvival signaling in various cancers (*30*). Together with CXCL12/CXCR4 signaling, direct cell-cell contact via VCAM-1/VLA-4 interactions may also be involved in enhancing leukemia survival by activating NF-κB signaling in leukemia, as revealed from our scRNA-seq analysis results and previous studies (*8*–*10*). To determine whether CXCL12 cytokine and VCAM-1/VLA-4 adhesive signaling axes enhance B-ALL survival via regulating downstream NF-κB signaling, we first compared the measured levels of NF-κB activation present in B-ALL cells cultured with or without niche cells using our leukemia-on-a-chip system and 2D culture (Fig. 4F and fig. S6). We found that BM niche cells significantly enhanced NF-κB nuclear translocation in B-ALL cells, as compared to those cultured in the absence of niche cells, which is consistent with our observance in the engineered human system (Fig. 1F). It was also determined that blocking both CXCL12/CXCR4 and VCAM-1/VLA-4 signaling axes using either CXCR4 inhibitor AMD3100 (AMD; Sigma-Aldrich) or VLA-4 inhibitor BIO suppressed the nuclear translocation of NF-κB in B-ALL cells (Fig. 4G). To further understand the importance of the niche-derived NF-κB signaling in

B-ALL survival, we assayed and compared B-ALL cell viability in the presence or absence of niche cells when blocking the NF-κB signaling with its inhibitor, BAY 11-7082 (BAY; EMD Millipore). Blocking NF-κB signaling in B-ALL cells significantly decreased B-ALL survival in the absence of niche cells, whereas coculture with niche cells partially rescued B-ALL cell survival from BAY treatment (Fig. 4H). These results together prove that cytokine signaling (CXCL12/CXCR4 axis) and adhesive signaling (VCAM-1/VLA-4 axis) between niche and B-ALL blasts may act to regulate downstream NF-κB signaling to promote B-ALL cell survival in the in vitro leukemic BM niche model.

To further confirm our observation, we applied our leukemia-on-a-chip for testing another four genetically different types of human B-ALL leukemia cell lines [i.e., NALM-6, 697, RS(4;11), and UOCB1], as well as three patient-derived samples (i.e., Ph^+ PAUZUW, Ph^+ 16-265, and non-Ph^+ 16-656). The results showed that after coculture with niche cells, NF-κB expression was significantly increased in human B-ALL cell lines (Fig. 4I) as well as in Ph^+ PAUZUW and 16-265 patient-derived B-ALL blasts, although it was not the case for non-Ph^+ 16-656 patient blasts (Fig. 4J). Together, these results suggested the enhanced NF-κB signaling as a general prosurvival mechanism contributed by niche cells.

Revealing the cellular and signaling heterogeneity in the leukemic BM niche

From the cytokine analysis, we observed that niche cells (ECs and MSCs) decreased CXCL12 secretion after prolonged coculture with B-ALL cells (Fig. 4, C and D). To understand whether murine ECs or MSCs or both cell types decrease CXCL12 secretion, we cultured ECs and MSCs, respectively, with B-ALL blasts for 2 days and monitored their cytokine secretion profiles using membrane-based ELISA and Western blotting assays. We found that ECs and MSCs differentially respond to the presence of B-ALL, whereas MSCs were more strongly affected by B-ALL blasts and had a reduced secretion of CXCL12 than ECs did (Fig. 5A and figs. S3 and S4).

We also studied whether ECs and MSCs all engaged in intercellular adhesive signaling, such as VCAM-1 or OPN, to promote B-ALL cell adhesion. We observed a significant increase of VCAM-1 expression but no significant change of OPN expression in ECs when cocultured with B-ALL cells (Fig. 5B and fig. S7, A and B). By contrast, coculture with B-ALL elicited a significant increase of OPN expression in MSCs (Fig. 5C). Moreover, we confirmed that OPN blockade can significantly decrease B-ALL adhesion onto MSCs, which was absent in ECs (fig. S6). By staining cells with proliferation marker, Ki67 (BioLegend, 652402), we demonstrated that a higher percentage of B-ALL cells interacting with MSCs were Ki67 negative, when compared to B-ALL interacting with ECs, suggesting that MSCs may promote B-ALL dormancy (fig. S8, A and B). We also assayed Ki67 expression in murine B-ALL and human leukemia cell lines on-chip cultured with and without niche cells, which demonstrated the heterogeneity across different types of B-ALL blasts (fig. S8, C to H). To study this further, B-ALL cells were labeled with the lipophilic dye, DiD, which is retained in dormant or slow-cycling cells in culture (*16*), and then cocultured with MSCs at a 1:1 ratio. It was found that B-ALL cells more physically close to MSCs tended to retain a higher intensity of DiD labeling, indicating that MSCs critically induced B-ALL dormancy (Fig. 5D). This finding was also confirmed by flow cytometric analysis (BD FACSymphony) with GFP (green fluorescent protein) as a gateway. The obtained result was analyzed using FlowJo (Tree Star, BD Biosciences), which showed a greater percentage of high DiD-retaining cells in B-ALL cells cocultured with MSCs compared to B-ALL cells cultured in isolation or with ECs (Fig. 5, E and F).

Historically, HSCs residing in either endosteal or medullary space (the peri-/vascular niche) show distinct niche-regulated cell fates (e.g., maintenance, proliferation, quiescence, and differentiation) (*14*). To further expand our understanding of how perivascular and endosteal niche cells differentially regulate leukemia progression, we co-seeded murine MC3T3 osteoblasts with B-ALL cells at 1:1 ratio in the outer ring area to encircle the medullary cavity, replicating the in vivo endosteal region (Fig. 1B and fig. S1). First, we characterized the adhesive signaling in osteoblasts in the presence or absence of B-ALL cells. We found that the presence of B-ALL cells slightly reduced mature osteoblast marker OPN expression in osteoblasts (fig. S7C), indicating that leukemia progression may inhibit osteoblast differentiation and maturation and be related to bone fracture or loss. Moreover, we compared the dormant status of B-ALL cell located in the perivascular and endosteal niches by characterizing its expression of p21 (Thermo Fisher Scientific, MA5-31479), a cyclin-dependent kinase inhibitor mediating cell cycle arrest (*32*). We observed that B-ALL cells in the endosteal niche had a higher number of p21-positive cells, in contrast to those in the perivascular niche (Fig. 5G). In parallel, we compared the viability of B-ALL cells in the two niches in response to 2-day treatment of three different drugs, including glucocorticoids, prednisone (PRE), microtubule inhibitor, VCR, and targeted agent capable of BCR-ABL1 inhibition, NIL (Fig. 5H and fig. S9). The results further confirmed a stronger dormancy and chemoresistance of B-ALL cells in the endosteal niche.

We also investigated the contributing mechanisms from hematopoietic cells. We cultured REH B-ALL blasts with primary human $CD34^+$ HSPCs (hematopoietic stem and progenitor cells) for over 1 week, during which hematopoietic stem and progenitor cells (HSPCs) may reestablish the hematopoietic environment following the previous protocol (*33*). The results showed that hematopoietic cells also promoted NF-κB activation in B-ALL cells and chemoresistance to VCR treatment (Fig. 5, I and J). Furthermore, we cultured healthy BM mononuclear cells with and without REH blasts in our leukemia systems for days 1 and 9 and quantified the number of $CD34^+$ cells. We observed that leukemia progression may impede the maintenance and/or expansion of hematopoietic progenitor cells (Fig. 5, K and L). Together, these findings highlight that BM niche cells, such as ECs, MSCs, and osteoblasts, may differentially contribute niche signaling to B-ALL blasts (Fig. 6A); for instance, ECs may enhance VCAM-1 singling to regulate B-ALL progression, while osteoblasts and MSCs may promote B-ALL dormancy via OPN signaling.

Eradicating leukemic burden by cotargeting leukemia niche signaling

To validate the preclinical utility of this platform and our mechanistic findings (Fig. 6A) in the niche-associated signaling for developing effective therapies, we screened a variety of combinational therapy by cotargeting tumor cell and niche-derived signaling to eradicate nonresponsive leukemia blasts or minimal residual disease burden, a major cause for refractory and relapsed leukemia. Initially, we assessed the efficacy of three treatment agents, i.e., PRE, VCR, and NIL. In the absence of niche cells, we observed efficient B-ALL eradication with all three agents in vitro; notably, the presence of niche cells resulted in the partial rescue of drug-induced cell death (Fig. 6B), consistent with previous observations (*34*, *35*).

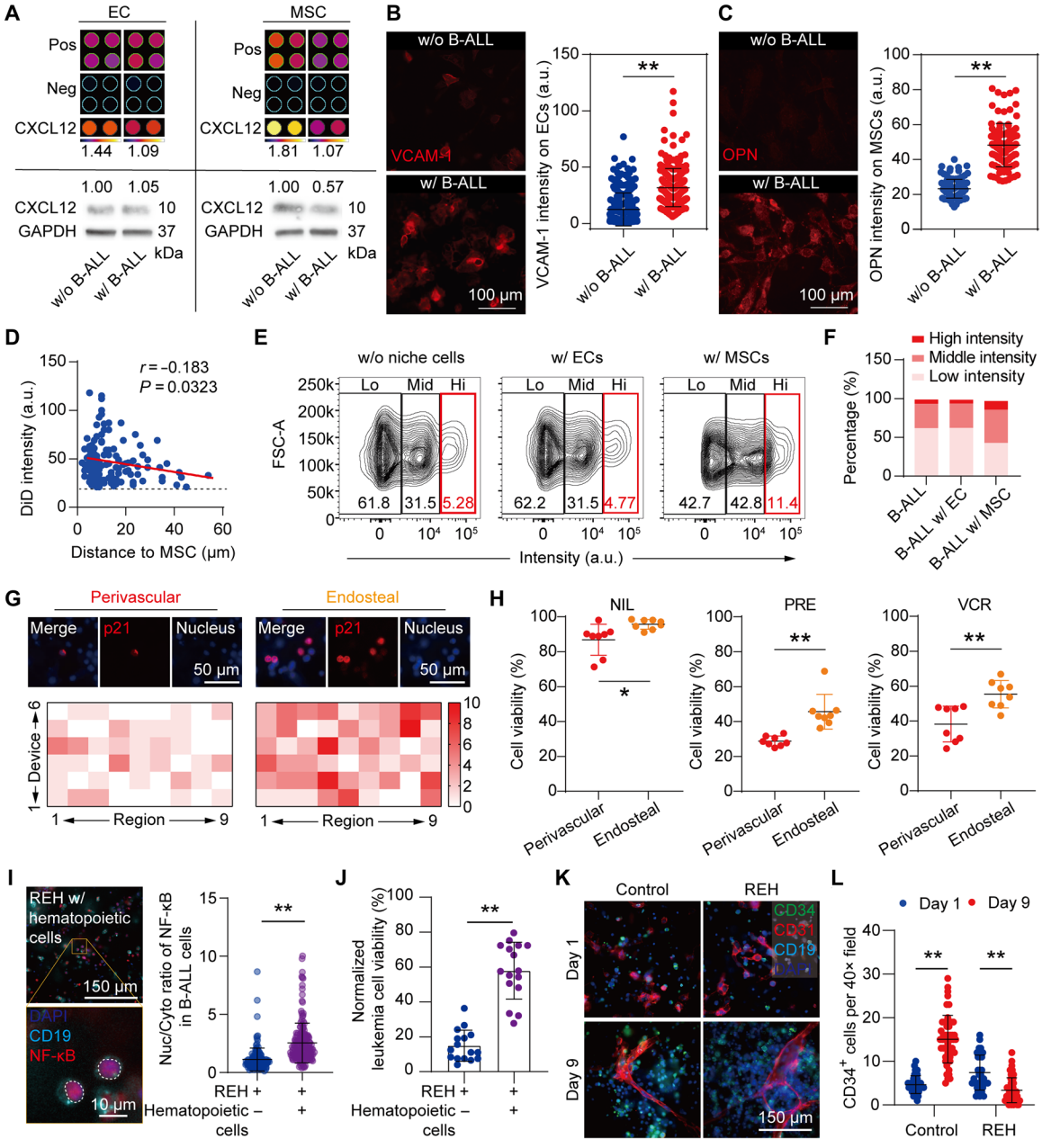

Fig. 5. Niche cells functioning disparately to regulate leukemia progression. (**A**) Membrane-based ELISA analysis of CXCL12 secretion of ECs (top left) and MSCs (top right). Western blotting of CXCL12 expression of ECs (bottom left) and MSCs (bottom right). (**B**) VCAM-1 expression of ECs and the quantification result ($n > 200$). (**C**) OPN expression of 2D cultured MSCs and the quantification result ($N > 200$). (**D**) The correlation between distance of B-ALL to MSCs and dye-retaining ability of B-ALL ($n > 120$). B-ALL with lower DiD intensity was excluded as indicated by the dashed line. (**E** and **F**) The flow cytometric images showing DiD dye retained in B-ALL, i.e., low (Lo), middle (Mid), and high (Hi) intensity. FSC-A, forward scatter area. (**G**) The representative images showing p21 expression in B-ALL located in the perivascular and endosteal niches ($N = 54$). (**H**) B-ALL viability in the two niches treated with different drugs. (**I**) NF-κB activation in REH after coculture with hematopoietic cells. (**J**) REH viability cultured with hematopoietic cells after 48-hour treatment of 20 nM VCR. (**K**) Representative images of $CD34^+$ HSPC within (REH) or without (Control) the leukemia niche at days 1 and 9. (**L**) Quantified number of $CD34^+$ cells. Unpaired *t* test (*$P < 0.05$ and **$P < 0.01$, Mann-Whitney test). GAPDH, glyceraldehyde-3-phosphate dehydrogenase; a.u., arbitrary units.

We then investigated whether cotargeting niche-derived prosurvival signals (CXCR4/CXCL12, VCAM-1/VLA-4, and NF-κB signaling) using either CXCR4 inhibitor (AMD), VLA-4 inhibitor (BIO), or NF-κB inhibitor (BAY) could improve the responsiveness of B-ALL–targeting chemotherapeutics. B-ALL blasts and niche cells (containing ECs and MSCs) were cocultured for 24 hours in the leukemia-on-a-chip, and then, we administered individual niche-targeting compounds in combination with either NIL, PRE, or VCR for 48 hours, after which B-ALL cell viability was measured. Notably, inhibiting CXCR4 and NF-κB signals significantly reversed the chemoprotective activity of niche cells exposed to tumor-targeting agents when compared to vehicle-, AMD-, and BAY-treated control groups, whereas VLA-4

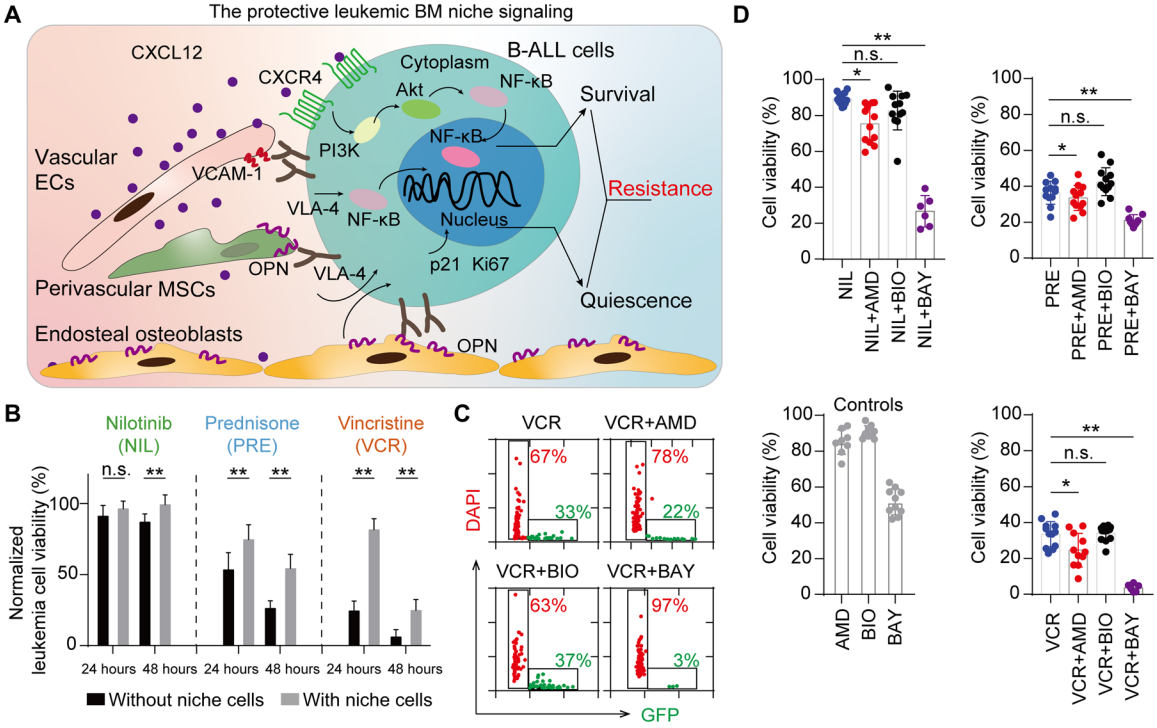

Fig. 6. On-chip testing of cotargeting niche signaling to eradicate leukemic burden. (**A**) The schematic of the protective leukemia BM niche regulating leukemia progression and quiescence via CXCL12/CXCR4 cytokine signaling and VCAM-1/VLA-4/OPN adhesive signaling. (**B**) The chemoresistance phenomenon was confirmed in the condition that B-ALL cells cultured in the leukemia BM niche were treated with three typical drugs (i.e., NIL, 1 μM; PRE, 1 μM; VCR, 0.1 μM) ($n = 6$). (**C**) Representative graphs showing quantified result corresponding to the VCR-treated groups in (**D**). The mean fluorescence intensity of GFP and DAPI of each B-ALL cell identified in ImageJ [National Institutes of Health (NIH)] was plotted after incubation at the respective conditions. (D) The graphs showed the percentage of B-ALL killing quantified for blockade of different niche singling. The respective control groups were AMD alone, BIO alone, and BAY alone treated groups. Data are means ± SD, collected from three individual experiments. One-way ANOVA followed by Tukey's post hoc test (*$P < 0.05$ and **$P < 0.01$). PI3K, phosphatidylinositol 3-kinase.

inhibition showed no significant effect on the responsiveness of B-ALL blasts to tumor-targeting agents (Fig. 6, C and D). The lack of response to VLA-4 treatment may be due to that VLA-4 blockade broke the leukemia dormancy to compensate the B-ALL death. This may also indicate a complex and redundant adhesive signaling between leukemia and niche cells, such as CD44 and E-selectin, as revealed in HSC niche and other types of leukemia (*36*, *37*).

DISCUSSION

In the present study, we engineered a biomimetic 3D microphysiological leukemia BM niche system for capturing the in vivo pathological features of human and murine B-ALL niche interactions and dissecting the underlying heterogeneous mechanisms regulated by niche cells to drive leukemia progression and chemoresistance. Unlike solid tumors, a comprehensive understanding of the leukemic BM niche remains in infancy (*20*). The healthy BM niche plays a vital role in regulating HSC fate and maintaining normal hematopoiesis, whereas in hematologic malignancies like acute leukemia, leukemic cells harness the BM niche to favor leukemia survival (*15*, *38*). Current in vitro studies adopt suspension cultures of primary leukemia cell lines to test therapeutics, but these simplified methods are clearly inadequate to mirror the complex conditions inside the 3D leukemic BM niche. Preclinical murine models allow for an in vivo study of the leukemia–BM niche interactions; however, in vivo complexity may affect reproducibility and accessibility of real-time monitoring of B-ALL interactions with its leukemic niche (*39*). Microfluidics-based microphysiological systems have been recently reported to reestablish the solid tumor microenvironments, yet limited attempts have been made to precisely replicate the in vivo anatomical structure of the leukemia BM niche and comparatively dissect the heterogeneous leukemia-niche interactions and chemoresistance mechanisms in B-ALL (*21*–*24*). Our in vitro engineered organotypic leukemia-on-a-chip is such a complementary platform to these preclinical models, as it functions as a bona fide replicate of the in vivo BM tissue architecture. Specifically, it provides several methodological advantages including the capability of control over various biological parameters (e.g., cell type, concentration and composition, tissue architectural information, and extracellular matrix properties), real-time visualization of physiological and pathophysiological dynamics (e.g., cell proliferation and migration, cell fate, and direct and indirect intercellular communications) modulated by internal factors and external stimuli, and the easy setup and compatibility with high-throughput on-chip biological assays (e.g., molecular, cellular, and histological characterizations) and follow-up cell retrieval for in-depth genetic analyses (e.g., scRNA-seq) (*19*, *24*).

Using this biomimetic niche model, we systematically explored the temporally dynamic interactions between B-ALL blasts and niche cells (i.e., vascular ECs, perivascular MSCs, and endosteal osteoblasts) and determined the distinct roles of different niche cells in regulating cytokine (e.g., CXCL12), intercellular adhesive signaling (e.g.,

VCAM-1 and OPN), and downstream B-ALL prosurvival NF-κB signaling, as well as cell proliferation (i.e., Ki67) and quiescence (i.e., p21) markers, which further demonstrated subtype-associated heterogeneity and treatment responses. The two divergent extrinsic cytokine and intercellular adhesive signaling mechanisms both enhanced downstream leukemia-intrinsic NF-κB signaling, supporting the notion that niche-derived signaling events promote B-ALL survival (*8*–*10*). Notably, other mechanisms of cytokine signaling may be included in regulating B-ALL progression; for instance, using conventional transwell-based studies, de Rooij *et al.* (*31*) found that CCR4/CCL2/CXCL22, CXCR1/2/IL8/GRO-1, and CXCR3/CXCL10 axes were involved in leukemia progression, which is also confirmed in our studies. Along with the cytokine signaling, adhesive signaling provided by the niche cells has been reported to promote leukemia progression and therapy resistance. We confirmed that ECs mainly promote leukemia survival via VCAM-1/VLA-4 axis, while MSCs and osteoblasts may induce leukemia dormancy via OPN signaling. Note that the BM microenvironment has a complex cellular composition and orchestrated interactions. The hematopoietic cells, such as monocyte, were also demonstrated to regulate the chemoresistance of B-ALL and other types of leukemia (*11*–*13*), which needs to be considered in detail to further improve the biomimicry of our system.

We also interrogated the spatial heterogeneity in the leukemic niche and found increased dormancy in B-ALL cells located at the endosteal niche relative to those in the perivascular niche, suggesting that BM subniches may differentially regulate leukemia progression, similar to the observances of its healthy counterpart (*14*, *40*). By comparing the engineered BM niches with six types of human B-ALL cells, as well as patient-derived samples, we revealed that NF-κB signaling is a general niche-derived mechanism to promote leukemia survival. With integration of scRNA-seq, we were able to generate a comprehensive map of the engineered human BM niche for different types of B-ALL blasts (e.g., favorable versus unfavorable), which underpinned that leukemia survival and quiescence across heterogeneous B-ALL subtypes is an orchestration between the microenvironmental cues and tumor genetics. Obtaining such a detailed profile via the biomimetic human leukemic BM stromal niche is of great importance since, to-date, it remains a challenge to map the in vivo counterpart because of the technical difficulties associated with isolating human BM stromal subpopulations in primary leukemic patient BM samples. The current leukemia-on-a-chip system, although not fully a replication of its in vivo counterpart, did provide a useful and powerful way to probe the evolving interactions between BM microenvironment and leukemia, which is presently not available with conventional methods and other blood cancer chips (*21*–*24*).

Recently, CAR T cells have emerged as a promising Food and Drug Administration–approved immunotherapy for relapsed and refractory B-ALL (*41*); however, patient responses are largely unpredictable. A detailed understanding of the leukemic BM immune niche is also indispensable for improving CAR T cell therapy. Future studies can be expanded on this model by increasing its biological complexity with addition of patient-derived cells, such as immune cells, to answer how the BM immune niche-derived regulatory signals influence leukemia progression and clinically relevant immune resistance, as well as other key BM niche components (e.g., hematopoietic cells), to interrogate how leukemia pathogenesis hampers normal hematopoiesis and how treatments may restore and maintain homeostasis. Additional work can be directed to recapitulate the biochemical (e.g., oxygen and cytokine gradients) and biophysical (e.g., ECM stiffness and sustained perfusion) cues in the in vivo leukemic BM niche, which may also be involved in regulating leukemia progression and therapy resistance (*17*, *42*).

In conclusion, we have demonstrated a unique organotypic leukemia-on-a-chip microphysiological system and comparatively and controllably dissected the heterogeneity of the leukemic BM niches in regulating B-ALL chemotherapy resistance. We believe that this bioengineered platform can be applied to many other hematological malignancies, for instance, AML, diffuse large B cell lymphoma, and multiple myeloma, as well as to study HSCs in a healthy BM niche, presenting an enabling tool for drug development and treatment testing under more physiologically relevant contexts.

MATERIALS AND METHODS

Cell culture

HUVECs (Lonza, C2519A) were cultured in EGM-2 Endothelial Cell Growth Medium-2 (Lonza, CC-3162). Human BM stem cells (hMSCs; Lonza, PT2501) were cultured in MSCGM Mesenchymal Stem Cell Growth Medium (Lonza, PT-3001). Human osteoblasts, hFOB 1.19 (hFOB, ATCC), were cultured using a 1:1 mixture of Ham's F12 medium and Dulbecco's modified Eagle's medium (DMEM/F12) with G418 (0.3 mg/ml; Corning) and 10% heat-inactivated fetal bovine serum (FBS; Invitrogen). All the primary cells were used in experiments between passages 3 and 8. Human cord blood $CD34^+$ cells (catalog no. 70008.5) and human BM mononuclear cells (catalog no. 70001.2) were purchased from STEMCELL Technologies and cultured in StemSpan SFEM II supplemented with StemSpan CC100. Human B-ALL cells [i.e., *EVT6-RUNX1* REH (ATCC), *MLL* RS(4;11) (ATCC), *E2A-PBX1* 697, *E2A-HLF* UOCB1, and NALM-6 (the Aifantis laboratory)] were cultured in RPMI 1640 medium (Gibco) supplemented with 10% FBS, and Ph^+ SUP-B15 cells (ATCC) in Iscove's modified Dulbecco's medium (IMDM; Gibco) with 15% FBS. Patient-derived sample (Ph^+ B-ALL blasts, PAUZUW) was provided by the Aifantis laboratory and sorted on the basis of $CD45^{lo/mid}$-$CD19^+CD10^+$ (*11*). Patient-derived samples (Ph^+ B-ALL blasts, 16-265, and non-Ph^+ B-ALL blasts, 16-656) were purchased from AMSBIO LLC and isolated using EasySep Release Human CD19 Positive Selection Kit (STEMCELL Technologies). Since multiple cells are cultured in the microfluidic system, the culture medium was used in a mixture (2:1:1:1) of HUVEC medium (EGM-2, Lonza), hMSCs medium (MSCGM, Lonza), hFOB medium (DMEM/F12), and human B-ALL cell medium (RPMI 1640 or IMDM, Gibco).

Murine EC line, C166 (ATCC), derived from mouse yolk sac, was grown in DMEM (Sigma-Aldrich), supplemented with 10% FBS and 1% penicillin-streptomycin. Murine MSC cell line, OP9 (ATCC), was grown in minimum essential medium–α (MEM-α; Thermo Fisher Scientific), supplemented with 20% FBS and 1% penicillin-streptomycin. Murine B-ALL cells was isolated from a well-characterized model of pediatric Ph^+ B-ALL (*27*), in which lethally irradiated C57BL/6 mice are reconstituted with retrovirally infected HSPCs cells ectopically coexpressing the B-ALL-associated P190 BCR-ABL1 isoform, as well as GFP for fluorescent cell tracing (Addgene plasmid no. 38185). Following the isolation, Ph^+ GFP^+ B-ALL cells were cultured and expanded in IMDM supplemented with 15% FBS, 1% penicillin-streptomycin, 100 μM L-glutamine, and 50 μM β-mercaptoethanol in a 37°C (with 5% CO_2) incubator. In addition,

to clearly distinguish the coexistence of ECs and MSCs, the two types of cells were prestained with CellTracker Red CMTPX Dye (Thermo Fisher Scientific; 10 μM in DMEM, 45 min) and DiD dye (Thermo Fisher Scientific; 1:200 dilution in MEM-α, 20 min), respectively, before being loaded into the device for the subsequent studies.

Hydrogel solutions

The gelatin solution (12 mg/ml) was prepared by dissolving gelatin powder from porcine skin (G2500, Sigma-Aldrich) in 1× Dulbecco's phosphate-buffered saline (DPBS; without calcium and magnesium; Invitrogen), warming, and vigorously stirring at 60°C for 30 min. The gelatin solution was then sterile-filtered, aliquot, and stored at 4°C for future use. The fibrinogen solution (6 mg/ml) was prepared by dissolving lyophilized fibrinogen from bovine plasma (F8630, Sigma-Aldrich) in DPBS at 37°C for 2 hours. The sterile-filtered fibrinogen solution was stored at 4°C for future use within 1 week. The thrombin solution was prepared by reconstituting lyophilized thrombin (604980, Sigma-Aldrich) in sterile DPBS to 100 U/ml and stored in aliquots at −20°C.

Device design, fabrication, and cell loading

The 3D microfluidics-based organotypic leukemia-on-a-chip device is composed of three distinct functional regions (fig. S1A): a central sinus region vascularized by ECs, an inner ring region serving as an interface of leukemia blasts (B-ALL cells) and niche cells (ECs and MSCs) interactions, and the outer ring channels (which is used to create the endosteal region by encapsulating osteoblasts and B-ALL cells within hydrogel), connected with four medium reservoirs, for cell culture medium supplies and waste removal. All the cell types were embedded in a fibrin hydrogel to maintain 3D cell culture. The microfluidic device was fabricated using standard soft lithography replica molding technique (*25*, *26*). Generally, the mold for the microfluidic device was fabricated with SU-8 negative photoresist (2050, MicroChem) at a thickness of 100 μm on a silicon wafer by using photolithography (fig. S1B). Before the replica molding process, the SU-8 mold was surface-modified by trichloro(1*H*,1*H*,2*H*,2*H*-perfluorooctyl) (448931, Sigma-Aldrich) vapor overnight in vacuum desiccation to facilitate later PDMS release. Then, a mixture of PDMS base and curing agent (SYLGARD 184, Dow Corning) at 10:1 weight-to-weight (w/w) ratio were mixed well, cast on the mold, degassed, and then solidified in an 80°C oven for 1 hour. Once PDMS was peeled from the mold, 1- and 3-mm holes were punched for three inlets and four medium reservoirs, respectively. The cleaned PDMS slabs were lastly bounded onto glass coverslips (22 mm by 22 mm; Thermo Fisher Scientific) to assemble the microfluidic device using oxygen plasma (PE-50 XL, Plasma Etch; 350 W, 2 min) and then incubated overnight in an 80°C oven for the recovery of hydrophobicity. The microfluidic devices were subsequently treated with ultraviolet for sterilization in a type 2 class laminar flow hood for 20 min. Afterward, B-ALL cells, ECs, and MSCs were embedded into 3D biomimetic hydrogels (fibrin, 3 mg/ml) (*43*), following a multistep loading protocol to seed ECs in the central sinus region and encapsulate B-ALL cells and niche cells (e.g., ECs and MSCs) in the medullary cavity region (fig. S1C). The seeding densities of ECs, MSCs, and B-ALL cells in medullary cavity region were 2.5×10^6, 2.5×10^6, and 5×10^6 cells/ml, respectively. To comparatively study the perivascular and endosteal niches, a mixture of osteoblasts and B-ALL cells (both at 5×10^6 cells/ml) in fibrin solution (3 mg/ml) was also loaded into the outer ring area to form the endosteal region and perivascular/endosteal niche interface. The cell-laden chips were cultured for 3 days, after which the morphology was analyzed by immunostaining. Note that the cell-laden chips for the human system were cultured for about 7 days. See the Supplementary Materials and fig. S1 for the detailed protocol.

Cell motility

GFP^+ B-ALL cells, C166 ECs, and OP9 MSCs were seeded in the biomimetic device and allowed to balance for 4 hours or culture for 48 hours at 37°C with 5% CO_2. After the defined incubation, the device was mounted on an inverted phase contrast microscope (Zeiss Axio Observer Z1) with a motorized stage and an environment control incubation chamber (Incubator XLmulti S1) to maintain 37°C with 5% CO_2. Phase contrast and fluorescent images were recorded every 5 min for 4 hours using a digital complementary metal-oxide semiconductor camera (ORCA-Flash4.0 LT, Hamamatsu Photonics) with a 20× objective. Each single cell was manually labeled in the continuous frames (in total, 49 frames) for 4 hours. Cell motility parameters were assessed via tracking of single B-ALL cell (60 cells per conditions) in ImageJ [National Institutes of Health (NIH)] using the Manual Tracking plug-in. Average cellular migration speed was defined by the distance traveled in a unit time calculated using the corresponding x and y coordinates at initial time t_{n-1} and end time t_n.

Immunoassays

Cytokine secretion profiles of niche cells were examined by using Mouse Cytokine Antibody Array membrane-based ELISA kit (AAM-CYT-3, RayBiotech) or Human Cytokine Antibody Array membrane-based ELISA kit (AAH-CYT-1, RayBiotech), according to the manufacturer's protocols. Briefly, supernatants were collected after 48-hour culture and centrifuged at 2000 rpm for 20 min at 4°C to remove cellular debris and then incubated overnight with Cytokine Antibody Array membranes. Biotinylated antibody cocktail was incubated with the membranes at 4°C overnight, followed by washing and incubation with horseradish peroxidase (HRP)–labeled streptavidin (1:1000) at 4°C overnight. Detection buffer C and D mixture (1:1) was then applied to visualize chemiluminescence for 2 min at room temperature (RT). Imaging was obtained by using a ChemiDoc Imaging System (Bio-Rad). Mean intensity of each spot was quantified in ImageJ (NIH) using the Protein Array Analyzer plug-in (written by G. Carpentier, Faculté des Sciences et Technologies, Université Paris, Paris, France).

Western blotting

Niche cells were cultured alone or cocultured with B-ALL cells for 3 days. The cells were lysed in radioimmunoprecipitation assay cell lysis buffer, supplemented with Halt Protease and Phosphatase Inhibitor Cocktail (1:100; Thermo Fisher Scientific) for 30 min on ice, and then centrifuged at 13,000 rpm for 20 min at 4°C, and the supernatant was stored at −80°C until assayed. Protein content was determined with Protein Quantification Kit-Rapid (51254, Sigma-Aldrich). Proteins (30 μg) were loaded on Mini-PROTEAN TGX Stain-Free Protein Gels (4568123, Bio-Rad) and then electroblotted onto polyvinylidene difluoride transfer membranes (1704156EDU, Bio-Rad). After blocking with 5% (w/v) nonfat dry milk in tris-buffered saline with 0.1% Tween 20 (TBST) for 1 hour at RT, the membranes were incubated overnight at 4°C with CXCL12 antibody (1:1000; 3740S, Cell Signaling Technology), with glyceraldehyde-3-phosphate dehydrogenase (1:1000; 2118S, Cell Signaling Technology) used as

a housekeeping gene. After washing three times with TBST for 30 min, the membranes were incubated for 1 hour at RT with a goat anti-rabbit immunoglobulin G HRP-conjugated polyclonal antibody (1:4000; Bio-Rad) and developed with a chemiluminescence enhancement kit (Clarity Max Western ECL Substrate, 1705061, Bio-Rad). Band densities were quantified from digital acquisition by a ChemiDoc Imaging System (Bio-Rad) in ImageJ (NIH) using the Gels plug-in.

Immunofluorescence staining

To investigate VCAM-1 and OPN expression level of murine ECs, MSCs, and osteoblasts in different conditions, the cells were respectively seeded onto a cover glass in 12-well plates (Falcon) and cocultured with B-ALL cells for 24 hours or infused into devices for 3D culture. Cells were fixed with 4% paraformaldehyde (15711, Electron Microscopy Sciences) for 30 min, permeabilized with 0.3% Triton X-100 (11332481001, Sigma-Aldrich) for 20 min, and then blocked with 3% bovine serum albumin for 1 hour on ice to prevent nonspecific binding. Cells were incubated with VCAM-1 (1:200; MAB2627, Millipore) and OPN (1:50; sc-20788, Santa Cruz Biotechnology) primary antibodies for 3 hours at RT or overnight at 4°C and then visualized with Alexa Fluor 555– or Alexa Fluor 647–conjugated secondary antibodies (Thermo Fisher Scientific). Cells were incubated for 10 min with 4′,6-diamidino-2-phenylindole (DAPI; Thermo Fisher Scientific) to counterstain nuclei.

Histopathology

The in vivo Ph^+ B-ALL murine model was generated using a previously published approach, and GFP^+ leukemic blasts were intravenously injected into nonirradiated C57BL/6 syngeneic recipient mice (*27*). When leukemic burden reached approximately 20% in total BM cells (about 12 days after transplantation), B-ALL recipient mice were sacrificed, and femurs were fixed overnight in 4% paraformaldehyde at 4°C. For hematoxylin and eosin (H&E) sectioning, fixed femurs were decalcified in 14% EDTA for 48 hours before being dehydrated in 70% ethanol and embedded in paraffin. Paraffin sections in 5 μm were stained with H&E for bright-field microscopy.

Drug resistance testing

The outcome of drugs was defined by the viability of B-ALL cells as a cytotoxic end point after drug treatment. B-ALL cells were cultured alone or cocultured with niche cells in 3D hydrogel devices for 24 hours and then incubated with 1 μM NIL (Cayman Chemical), 1 μM PRE (Sigma-Aldrich), and 0.1 μM VCR (Sigma-Aldrich) for 48 hours. The cell viability was quantitatively determined by using Calcein-AM (Thermo Fisher Scientific) and DAPI, which stained the live and dead cells, respectively. Briefly, cells were rinsed thrice with PBS and incubated with Calcein-AM and DAPI (1 and 5 μg/ml in PBS or medium) solution for 30 min at 37°C, followed by a final rinse with PBS. Afterward, cells were observed under a fluorescence microscope, and cellular viability was quantitatively measured by counting the number of objects in the green (live cells) and red (dead cells) channels. Untreated groups of B-ALL cells were used as controls to benchmark the drug resistance of different groups.

Combinational drug regimens

The 3D biomimetic leukemic niche model was exploited to test the combinational drug regimens in vitro. Generally, the murine leukemic niche models were cultured for 24 hours after fabrication, then respectively administrated with various pharmaceuticals [i.e., AMD (5 μg/ml), BIO (1 μg/ml), and 10 μM BAY, correspondingly], and concomitantly treated with 1 μM NIL, 1 μM PRE, or 0.1 μM VCR for 48 hours. The viability of B-ALL cells was measured by the DAPI staining as described above.

scRNA-seq

The leukemia BM niche samples (designated as B-ALL-Niche, B-ALL cocultured with niche cells) and control groups of leukemia culture alone (B-ALL alone) and niche cell (HUVEC, hMSCs, and hFOB) culture without leukemia (niche alone) were engineered and cultured on-chip for 7 days as described above. Single-cell suspensions of B-ALL samples were prepared by off-chip recovery with nattokinase [50 FU (fibrinolytic unit)/ml] (*43*) and prelabeled with different anti-human hashtag antibodies (TotalSeq, BioLegend) and mixed into two samples, REH BM niche and SUP BM niche. The libraries were prepared using the Chromium Single Cell 3he librar Kits (v3) [Single Cell 3ingle Cel & Gel Bead Kit v3 (PN-1000075), Single Cell 3gle it Kit v3 (PN-1000073), and i7 Multiplex Kit (PN-120262) (10x Genomics)] and following the Single Cell 3and follo Kits (v3) User Guide (manual part no. CG000183 Rev B). Libraries were then run on an Illumina NovaSeq 6000 using 28–base pair (bp) read 1, 8-bp i7 index, and 91-bp read 2.

Sequencing results were demultiplexed and converted to FASTQ format using Illumina bcl2fastq software, followed by sample demultiplexing, barcode processing, and single-cell 3′ gene counting with Cell Ranger v3.1 (10x Genomics). The cDNA insert was aligned to the hg38/GRCh38 reference genome. Further analysis including quality control and data filtering, the identification of highly variable genes, dimensionality reduction, standard unsupervised clustering algorithms, and the discovery of differentially expressed genes was performed using the Seurat toolkit (*44*). For data visualization, uniform manifold approximation and projection dimensionality reduction was lastly applied (*45*). See the Supplementary Materials for the detailed protocol.

Statistics

Data were first analyzed for normality and then compared with unpaired *t* test or one-way analysis of variance (ANOVA) using Prism8.0 (GraphPad). $*P < 0.05$ and $**P < 0.01$ were considered significantly different. The results, including the error bars in the graphs, were given as means ± SD. Details are reported in each figure.

SUPPLEMENTARY MATERIALS

Supplementary material for this article is available at http://advances.sciencemag.org/cgi/content/full/6/44/eaba5536/DC1

View/request a protocol for this paper from *Bio-protocol*.

REFERENCES AND NOTES

1. C. H. Pui, L. L. Robison, A. T. Look, Acute lymphoblastic leukaemia. *Lancet* **371**, 1030–1043 (2008).
2. S. P. Hunger, C. G. Mullighan, Acute lymphoblastic leukemia in children. *N. Engl. J. Med.* **373**, 1541–1552 (2015).
3. T. Terwilliger, M. Abdul-Hay, Acute lymphoblastic leukemia: A comprehensive review and 2017 update. *Blood Cancer J.* **7**, e577 (2017).
4. M. L. Churchman, J. Low, C. Qu, E. M. Paietta, L. H. Kasper, Y. Chang, D. Payne-Turner, M. J. Althoff, G. Song, S.-C. Chen, J. Ma, M. Rusch, D. M. Goldrick, M. Edmonson, P. Gupta, Y.-D. Wang, W. Caufield, B. Freeman, L. Li, J. C. Panetta, S. Baker, Y.-L. Yang, K. G. Roberts, K. M. Castlain, I. Iacobucci, J. L. Peters, V. E. Centonze, F. Notta, S. M. Dobson, S. Zandi, J. E. Dick, L. Janke, J. Peng, K. Kodali, V. Pagala, J. Min, A. Mayasundari, R. T. Williams, C. L. Willman, J. Rowe, S. Luger, R. A. Dickins, R. K. Guy, T. Chen, C. G. Mullighan, Efficacy

of retinoids in IKZF1-mutated BCR-ABL1 acute lymphoblastic leukemia. *Cancer Cell* **28**, 343–356 (2015).
5. T. Schmidt, P. Carmeliet, Angiogenesis: A target in solid tumors, also in leukemia? *Hematology Am. Soc. Hematol. Educ. Program* **2011**, 1–8 (2011).
6. D. Passaro, M. Irigoyen, C. Catherinet, S. Gachet, C. D. C. De Jesus, C. Lasgi, C. T. Quang, J. Ghysdael, CXCR4 is required for leukemia-initiating cell activity in T cell acute lymphoblastic leukemia. *Cancer Cell* **27**, 769–779 (2015).
7. L. A. Pitt, A. N. Tikhonova, H. Hu, T. Trimarchi, B. King, Y. Gong, M. Sanchez-Martin, A. Tsirigos, D. R. Littman, A. A. Ferrando, S. J. Morrison, D. R. Fooksman, I. Aifantis, S. R. Schwab, CXCL12-producing vascular endothelial niches control acute T cell leukemia maintenance. *Cancer Cell* **27**, 755–768 (2015).
8. B. Boyerinas, M. Zafrir, A. E. Yesilkanal, T. T. Price, E. M. Hyjek, D. A. Sipkins, Adhesion to osteopontin in the bone marrow niche regulates lymphoblastic leukemia cell dormancy. *Blood* **121**, 4821–4831 (2013).
9. R. Jacamo, Y. Chen, Z. Wang, W. Ma, M. Zhang, E. L. Spaeth, Y. Wang, V. L. Battula, P. Y. Mak, K. Schallmoser, P. Ruvolo, W. D. Schober, E. J. Shpall, M. H. Nguyen, D. Strunk, C. E. Bueso-Ramos, S. Konoplev, R. E. Davis, M. Konopleva, M. Andreeff, Reciprocal leukemia-stroma VCAM-1/VLA-4-dependent activation of NF-κB mediates chemoresistance. *Blood* **123**, 2691–2702 (2014).
10. Y.-T. Hsieh, E. J. Gang, H. Geng, E. Park, S. Huantes, D. Chudziak, K. Dauber, P. Schaefer, C. Scharman, H. Shimada, S. Shojaee, L. Klemm, R. Parameswaran, M. Loh, E.-S. Kang, H. H. Koo, W.-K. Hofmann, J. Andrade, G. M. Crooks, C. L. Willman, M. Müschen, T. Papayannopoulou, N. Heisterkamp, H. Bönig, Y.-M. Kim, Integrin alpha4 blockade sensitizes drug resistant pre-B acute lymphoblastic leukemia to chemotherapy. *Blood* **121**, 1814–1818 (2013).
11. M. T. Witkowski, I. Dolgalev, N. A. Evensen, C. Ma, T. Chambers, K. G. Roberts, S. Sreeram, Y. Dai, A. N. Tikhonova, A. Lasry, C. Qu, D. Pei, C. Cheng, G. A. Robbins, J. Pierro, S. Selvaraj, V. Mezzano, M. Daves, P. J. Lupo, M. E. Scheurer, C. A. Loomis, C. G. Mullighan, W. Chen, K. R. Rabin, A. Tsirigos, W. L. Carroll, I. Aifantis, Extensive remodeling of the immune microenvironment in B cell acute lymphoblastic leukemia. *Cancer Cell* **37**, 867–882.e12 (2020).
12. Y. Lee, M. Chittezhath, V. André, H. Zhao, M. Poidinger, A. Biondi, G. D'Amico, S. K. Biswas, Protumoral role of monocytes in human B-cell precursor acute lymphoblastic leukemia: Involvement of the chemokine CXCL10. *Blood* **119**, 227–237 (2012).
13. P. Giannoni, G. Pietra, G. Travaini, R. Quarto, G. Shyti, R. Benelli, L. Ottaggio, M. C. Mingari, S. Zupo, G. Cutrona, I. Pierri, E. Balleari, A. Pattarozzi, M. Calvaruso, C. Tripodo, M. Ferrarini, D. de Totero, Chronic lymphocytic leukemia nurse-like cells express hepatocyte growth factor receptor (c-MET) and indoleamine 2,3-dioxygenase and display features of immunosuppressive type 2 skewed macrophages. *Haematologica* **99**, 1078–1087 (2014).
14. L. Ding, S. J. Morrison, Haematopoietic stem cells and early lymphoid progenitors occupy distinct bone marrow niches. *Nature* **495**, 231–235 (2013).
15. C.-W. Duan, J. Shi, J. Chen, B. Wang, Y.-H. Yu, X. Qin, X.-C. Zhou, Y.-J. Cai, Z.-Q. Li, F. Zhang, M.-Z. Yin, Y. Tao, J.-Q. Mi, L.-H. Li, T. Enver, G.-Q. Chen, D.-L. Hong, Leukemia propagating cells rebuild an evolving niche in response to therapy. *Cancer Cell* **25**, 778–793 (2014).
16. S. Ebinger, E. Z. Özdemir, C. Ziegenhain, S. Tiedt, C. C. Alves, M. Grunert, M. Dworzak, C. Lutz, V. A. Turati, T. Enver, H.-P. Horny, K. Sotlar, S. Parekh, K. Spiekermann, W. Hiddemann, A. Schepers, B. Polzer, S. Kirsch, M. Hoffmann, B. Knapp, J. Hasenauer, H. Pfeifer, R. Panzer-Grümayer, W. Enard, O. Gires, I. Jeremias, Characterization of rare, dormant, and therapy-resistant cells in acute lymphoblastic leukemia. *Cancer Cell* **30**, 849–862 (2016).
17. D. Duarte, E. D. Hawkins, O. Akinduro, H. Ang, K. De Filippo, I. Y. Kong, M. Haltalli, N. Ruivo, L. Straszkowski, S. J. Vervoort, C. M. Lean, T. S. Weber, R. Khorshed, C. Pirillo, A. Wei, S. K. Ramasamy, A. P. Kusumbe, K. Duffy, R. H. Adams, L. E. Purton, L. M. Carlin, C. L. Celso, Inhibition of endosteal vascular niche remodeling rescues hematopoietic stem cell loss in AML. *Cell Stem Cell* **22**, 64–77.e6 (2018).
18. E. D. Hawkins, D. Duarte, O. Akinduro, R. A. Khorshed, D. Passaro, M. Nowicka, L. Straszkowski, M. K. Scott, S. Rothery, N. Ruivo, K. Foster, M. Waibel, R. W. Johnstone, S. J. Harrison, D. A. Westerman, H. Quach, J. Gribben, M. D. Robinson, L. E. Purton, D. Bonnet, C. L. Celso, T-cell acute leukaemia exhibits dynamic interactions with bone marrow microenvironments. *Nature* **538**, 518–522 (2016).
19. S. N. Bhatia, D. E. Ingber, Microfluidic organs-on-chips. *Nat. Biotechnol.* **32**, 760–772 (2014).
20. D. Duarte, E. D. Hawkins, C. C. Lo, The interplay of leukemia cells and the bone marrow microenvironment. *Blood* **131**, 1507–1511 (2018).
21. Y. Zheng, Y. Sun, X. Yu, Y. Shao, P. Zhang, G. Dai, J. Fu, Angiogenesis in liquid tumors: An in vitro assay for leukemic-cell-induced bone marrow angiogenesis. *Adv. Healthc. Mater.* **5**, 1014–1024 (2016).
22. R. G. Mannino, A. N. Santiago-Miranda, P. Pradhan, Y. Qiu, J. C. Mejias, S. S. Neelapu, K. Roy, W. A. Lam, 3D microvascular model recapitulates the diffuse large B-cell lymphoma tumor microenvironment in vitro. *Lab Chip* **17**, 407–414 (2017).
23. A. Bruce, R. Evans, R. Mezan, L. Shi, B. S. Moses, K. H. Martin, L. F. Gibson, Y. Yang, Three-dimensional microfluidic tri-culture model of the bone marrow microenvironment for study of acute lymphoblastic leukemia. *PLOS ONE* **10**, e0140506 (2015).
24. W. Zhang, W. Y. Lee, D. S. Siegel, P. Tolias, J. Zilberberg, Patient-specific 3D microfluidic tissue model for multiple myeloma. *Tissue Eng. Part C Methods* **20**, 663–670 (2014).
25. C. Ma, L. Zhao, E.-M. Zhou, J. Xu, S. Shen, J. Wang, On-chip construction of liver lobule-like microtissue and its application for adverse drug reaction assay. *Anal. Chem.* **88**, 1719–1727 (2016).
26. C. Ma, C. Tian, L. Zhao, J. Wang, Pneumatic-aided micro-molding for flexible fabrication of homogeneous and heterogeneous cell-laden microgels. *Lab Chip* **16**, 2609–2617 (2016).
27. S. Li, R. L. Ilaria Jr., R. P. Million, G. Q. Daley, R. A. Van Etten, The P190, P210, and P230 forms of the *BCR/ABL* oncogene induce a similar chronic myeloid leukemia-like syndrome in mice but have different lymphoid leukemogenic activity. *J. Exp. Med.* **189**, 1399–1412 (1999).
28. A. N. Tikhonova, I. Dolgalev, H. Hu, K. K. Sivaraj, E. Hoxha, Á. Cuesta-Domínguez, S. Pinho, I. Akhmetzyanova, J. Gao, M. Witkowski, M. Guillamot, M. C. Gutkin, Y. Zhang, C. Marier, C. Diefenbach, S. Kousteni, A. Heguy, H. Zhong, D. R. Fooksman, J. M. Butler, A. Economides, P. S. Frenette, R. H. Adams, R. Satija, A. Tsirigos, I. Aifantis, The bone marrow microenvironment at single-cell resolution. *Nature* **569**, 222–228 (2019).
29. E. A. R. Sison, D. Magoon, L. Li, C. E. Annesley, R. E. Rau, D. Small, P. Brown, Plerixafor as a chemosensitizing agent in pediatric acute lymphoblastic leukemia: Efficacy and potential mechanisms of resistance to CXCR4 inhibition. *Oncotarget* **5**, 8947–8958 (2014).
30. E. J. English, S. A. Mahn, A. Marchese, Endocytosis is required for CXC chemokine receptor type 4 (CXCR4)-mediated Akt activation and antiapoptotic signaling. *J. Biol. Chem.* **293**, 11470–11480 (2018).
31. B. de Rooij, R. Polak, L. C. J. van den Berk, F. Stalpers, R. Pieters, M. L. den Boer, Acute lymphoblastic leukemia cells create a leukemic niche without affecting the CXCR4/CXCL12 axis. *Haematologica* **102**, e389–e393 (2017).
32. T. Abbas, A. Dutta, p21 in cancer: Intricate networks and multiple activities. *Nat. Rev. Cancer* **9**, 400–414 (2009).
33. D. B. Chou, V. Frismantas, Y. Milton, R. David, P. Pop-Damkov, D. Ferguson, A. M. Donald, Ö. V. Bölükbaşı, C. E. Joyce, L. S. M. Teixeira, A. Rech, A. Jiang, E. Calamari, S. Jalili-Firoozinezhad, B. A. Furlong, L. R. O'Sullivan, C. F. Ng, Y. Choe, S. Marquez, K. C. Myers, O. K. Weinberg, R. P. Hasserjian, R. Novak, O. Levy, R. Prantil-Baun, C. D. Novina, A. Shimamura, L. Ewart, D. E. Ingber, On-chip recapitulation of clinical bone marrow toxicities and patient-specific pathophysiology. *Nat. Biomed. Eng.* **4**, 394–406 (2020).
34. R. Polak *et al.*, B-cell precursor acute lymphoblastic leukemia cells use tunneling nanotubes to orchestrate their microenvironment. *Blood* **126**, 2404–2414 (2015).
35. R. Maffei, S. Fiorcari, J. Bulgarelli, S. Martinelli, I. Castelli, S. Deaglio, G. Debbia, M. Fontana, V. Coluccio, G. Bonacorsi, P. Zucchini, F. Narni, G. Torelli, M. Luppi, R. Marasca, Physical contact with endothelial cells through β1- and β2- integrins rescues chronic lymphocytic leukemia cells from spontaneous and drug-induced apoptosis and induces a peculiar gene expression profile in leukemic cells. *Haematologica* **97**, 952–960 (2012).
36. I. G. Winkler, V. Barbier, B. Nowlan, R. N. Jacobsen, C. E. Forristal, J. T. Patton, J. L. Magnani, J.-P. Lévesque, Vascular niche E-selectin regulates hematopoietic stem cell dormancy, self renewal and chemoresistance. *Nat. Med.* **18**, 1651–1657 (2012).
37. L. Jin, K. J. Hope, Q. Zhai, F. Smadja-Joffe, J. E. Dick, Targeting of CD44 eradicates human acute myeloid leukemic stem cells. *Nat. Med.* **12**, 1167–1174 (2006).
38. A. Colmone, M. Amorim, A. L. Pontier, S. Wang, E. Jablonski, D. A. Sipkins, Leukemic cells create bone marrow niches that disrupt the behavior of normal hematopoietic progenitor cells. *Science* **322**, 1861–1865 (2008).
39. C.-P. Day, G. Merlino, T. Van Dyke, Preclinical mouse cancer models: A maze of opportunities and challenges. *Cell* **163**, 39–53 (2015).
40. S. Pinho, T. Marchand, E. Yang, Q. Wei, C. Nerlov, P. S. Frenette, Lineage-biased hematopoietic stem cells are regulated by distinct niches. *Dev. Cell* **44**, 634–641.e4 (2018).
41. J. H. Park, I. Rivière, M. Gonen, X. Wang, B. Sénéchal, K. J. Curran, C. Sauter, Y. Wang, B. Santomasso, E. Mead, M. Roshal, P. Maslak, M. Davila, R. J. Brentjens, M. Sadelain, Long-term follow-up of CD19 CAR therapy in acute lymphoblastic leukemia. *N. Engl. J. Med.* **378**, 449–459 (2018).
42. J. S. Choi, B. A. Harley, Marrow-inspired matrix cues rapidly affect early fate decisions of hematopoietic stem and progenitor cells. *Sci. Adv.* **3**, e1600455 (2017).
43. B. Carrion, I. A. Janson, Y. P. Kong, A. J. Putnam, A safe and efficient method to retrieve mesenchymal stem cells from three-dimensional fibrin gels. *Tissue Eng. Part C Methods* **20**, 252–263 (2014).
44. A. Butler, P. Hoffman, P. Smibert, E. Papalexi, R. Satija, Integrating single-cell transcriptomic data across different conditions, technologies, and species. *Nat. Biotechnol.* **36**, 411–420 (2018).

45. E. Becht, L. M. Innes, J. Healy, C.-A. Dutertre, I. W. H. Kwok, L. G. Ng, F. Ginhoux, E. W. Newell, Dimensionality reduction for visualizing single-cell data using UMAP. *Nat. Biotechnol.* (2018).

Acknowledgments

Funding: This work was supported by the NSF (CBET 1701322), the U.S. NIH [R21EB025406, R35GM133646, RO1CA202025, RO1CA202027, RO1CA216421, 1RO1CA228135, and PO1CA229086), the Leukemia & Lymphoma Society (TRP#6580), the New York State Department of Health (NYSTEM Program), and the St. Baldrick's Cancer Research Foundation (I.A). M.T.W. is a Fellow of The Leukemia & Lymphoma Society. We would like to thank the NYU School of Medicine core facilities including High Performance Computing and the Genome Technology Center (this shared resource is partially supported by the Cancer Center Support Grant P30CA016087 at the Laura and Isaac Perlmutter Cancer Center). **Author contributions:** C.M. and W.C. conceived the project. C.M., M.T.W., I.A., and W.C. designed the experiments. C.M., M.T.W., J.H., S.S., W.Q., J.T., and X.C. performed experiments. C.M., M.T.W., I.D., and W.C. analyzed data. C.M. and W.C. wrote the manuscript. I.A. and W.C. supervised the project. All authors edited and approved the final manuscript. **Competing interests:** The authors declare that they have no competing interests. **Data and materials availability:** All data needed to evaluate the conclusions in the paper are present in the paper and/or the Supplementary Materials. Additional data related to this paper may be requested from the authors. The scRNA-seq data are available in the Gene Expression Omnibus (GEO) under accession number GSE138811.

Submitted 12 December 2019
Accepted 10 September 2020
Published 30 October 2020
10.1126/sciadv.aba5536

Citation: C. Ma, M. T. Witkowski, J. Harris, I. Dolgalev, S. Sreeram, W. Qian, J. Tong, X. Chen, I. Aifantis, W. Chen, Leukemia-on-a-chip: Dissecting the chemoresistance mechanisms in B cell acute lymphoblastic leukemia bone marrow niche. *Sci. Adv.* **6**, eaba5536 (2020).

Science Advances

Leukemia-on-a-chip: Dissecting the chemoresistance mechanisms in B cell acute lymphoblastic leukemia bone marrow niche

Chao Ma, Matthew T. Witkowski, Jacob Harris, Igor Dolgalev, Sheetal Sreeram, Weiyi Qian, Jie Tong, Xin Chen, Iannis Aifantis and Weiqiang Chen

Sci Adv **6** (44), eaba5536.
DOI: 10.1126/sciadv.aba5536